

TriSweep: A Four-Drone Swarm Framework for Electromagnetic Side-Channel Analysis

Eric Yocam^{*1} and Varghese Vaidyan²

¹Department of Computer Science, College of Engineering, California Polytechnic
State University, San Luis Obispo, CA 93407, USA

²Beacom College of Computer and Cyber Sciences, Dakota State University, Madison,
SD 57042, USA

May 22, 2026

Abstract

Electromagnetic (EM) side-channel analysis traditionally assumes a stationary, close-proximity probe—a threat model that underestimates aerial adversaries. *TriSweep* is a simulation framework that designs and evaluates a four-drone swarm architecture for autonomous standoff EM-SCA of embedded microcontrollers at 0.25–1.5 m. Three spatially specialized collector drones—Anchor (full-spectrum), Mask Probe (mask-register loading leakage), and Cipher Probe (masked SubBytes output leakage)—feed a stationary Accumulator drone that performs coherent combining (+4.8 dB SNR gain) and second-order mask cancellation via a centered product of the two spatially separated leakage streams. Evaluated against three real ANSSI ASCAD datasets (ATmega8515 masked AES-128 and 50/100-sample desynchronized variants), the framework achieves a simulated key rank 18 ± 1.7 (five-seed) at 0.25 m on the primary masked dataset. Profiling-trace cross-correlation alignment reduces the single-drone rank from 89 to 21 on the 100-sample-jitter variant, demonstrating compensation for drone hover vibration. A two-channel CNN in the Accumulator converges to a loss of 0.454 (vs. random baseline 5.545) and improves rank on desynchronized datasets. No physical hardware has been fabricated; prototype construction is the planned next step.

Keywords: electromagnetic side-channel analysis, drone swarm, software-defined radio, coherent combining, second-order attack, mask cancellation, template attack, AES, autonomous systems

1 Introduction

This paper presents *TriSweep*, a simulation framework for four-drone swarm electromagnetic side-channel analysis of masked embedded cryptographic devices at standoff distances of 0.25–1.5 m. The following subsections establish the threat landscape that motivates the work, the technical challenges it addresses, and the framework’s design and key results.

^{*}Corresponding author: eyocam@calpoly.edu

1.1 Background and Threat Landscape

Electromagnetic (EM) side-channel analysis exploits unintended radiation emitted during cryptographic computation to recover secret keys without physical access to the target device [1, 2]. Since Gandolfi *et al.* [1] first demonstrated key recovery from smart cards in 2001, the attack surface has widened considerably: the field has advanced from simple power traces [3, 4] through correlation-based methods [5], template attacks [6], second-order analysis [7, 8], and deep learning-based profiling [9, 10]. AES-128 executing on embedded microcontrollers remains the canonical target [11], and the breadth of vulnerable platforms—from smart cards and IoT sensors to industrial control modules—makes the threat operationally significant for critical infrastructure.

A persistent and increasingly questionable assumption underpins nearly all of this work: the adversary places a near-field probe at millimeter-to-centimeter distances from the target. Physical proximity guards appear to provide meaningful protection under this model. A device mounted behind a locked panel, inside an enclosure, or across a room is considered safe from EM analysis precisely because bringing a loop antenna close enough requires access that the security perimeter is designed to deny. This assumption is becoming untenable. Commercial off-the-shelf (COTS) unmanned aerial vehicles now routinely carry payloads exceeding 500 g at costs below \$2,000 [12], software-defined radio hardware spans 70 MHz to 6 GHz for under \$300 [13], and custom low-noise amplifier modules achieve sub-2 dB noise figure across 1–500 MHz within the weight and power budgets of a small hexacopter payload [14]. An adversary who can fly a drone within 0.25–1.5 m of a target’s exterior surface — past a window, over a perimeter fence, or beneath a server room air duct — bypasses all proximity-based physical security measures without requiring any physical contact or facility access [15, 16].

1.2 Technical Motivation

Array signal processing theory [17] predicts that coherently combining N receivers improves SNR by a factor of N , corresponding to $10 \log_{10}(3) \approx 4.8$ dB for three receivers. Realizing this gain across multiple airborne platforms requires sub-nanosecond inter-drone clock synchronization and precise relative positioning — challenges that recent advances in GPS-disciplined oscillators and visual-inertial odometry now make tractable at COTS price points. The combination of aerial mobility, multi-receiver coherent gain, and autonomous repositioning creates a qualitatively new threat vector with no direct precedent in the published EM-SCA literature.

A further complication is that modern embedded implementations do not execute AES-128 in the clear. First-order masking schemes [8] randomize each intermediate value v with a fresh random mask r , computing $v \oplus r$ instead of v directly. Defeating first-order masking requires second-order analysis [7]: the adversary must jointly observe the mask-loading leakage event and the masked-computation leakage event, which occur at different points in time within the same execution. In a single-receiver system these two events must be separated algorithmically from one trace, a process that is sensitive to timing jitter and implementation noise [18]. The spatial decomposition insight underlying *TriSweep* is that dedicated collector drones can be positioned and SNR-weighted to specialize in each leakage event — Drone B for the mask-register loading window and Drone C for the masked SubBytes output window — so that their centered product at the Accumulator (Drone D) cancels the mask without algorithmic preprocessing or knowledge of the mask value.

1.3 The *TriSweep* Framework

TriSweep is a simulation framework that designs, implements, and evaluates this four-drone architecture. All experimental results derive from real published ASCAD EM datasets [19] combined with a physics-based free-space path-loss noise model; no drone hardware has been fabricated or flown. The simulation framework serves two purposes: (1) it provides a quantitative prediction of what a physical system achieving the modeled SNR would accomplish against real masked AES-128 leakage; and (2) it establishes the algorithms, protocols, and combining pipelines that a physical implementation would need to realize, giving a concrete design specification for the prototype construction phase. Evaluated against three real ANSSI ASCAD datasets — the primary ATmega8515 masked AES-128 database and desynchronized variants with 50- and 100-sample acquisition jitter — the framework achieves simulated key rank 18 ± 1.7 (five-seed statistical validation) at 0.25 m standoff, a tenfold improvement over the single-drone baseline rank of 197.

1.4 Contributions

1. A four-drone EM-SCA platform design: Drone A (Anchor), Drone B (Mask Probe), Drone C (Cipher Probe), and Drone D (Accumulator). *All results use real ASCAD datasets and a simulated standoff noise model; no hardware has been fabricated.*
2. A swarm consensus protocol for EM-optimal repositioning via distributed Fisher information maximization, 200 ms cycles.
3. A two-stage inter-drone clock synchronization protocol targeting <10 ns jitter.
4. Profiling-trace cross-correlation alignment: key rank reduces from 89 to 21 on the 100-sample-jitter ASCAD dataset.
5. Drone D second-order combining via a centered product of Drones B and C streams, reducing simulated key rank to 18 ± 1.7 .
6. First published aerial, multi-node, autonomous EM-SCA framework with hardware second-order mask cancellation design.

The remainder of the paper is organized as follows. Section 2 surveys related work and positions *TriSweep* against the state of the art. Section 3 establishes the physical signal model and threat assumptions. Section 4 describes the four-drone architecture and all seven algorithms. Section 5 details the experimental methodology. Section 6 presents simulation results. Section 7 discusses design trade-offs, operational factors, limitations, and future work. Section 8 concludes.

2 Related Work

This section surveys four bodies of literature that directly motivate *TriSweep*: classical EM side-channel attacks, second-order analysis, deep learning-based profiling, and mobile threat models. Section 2.5 closes the survey with a structured comparison positioning *TriSweep* against recent work.

2.1 Electromagnetic Side-Channel Analysis

Quisquater and Samyde [20] introduced EM analysis; Gandolfi *et al.* [1] provided the first key-recovery demonstrations. Agrawal *et al.* [2] characterized multiple EM side channels; Messerges *et al.* [21] evaluated smart-card security under power and EM threats. Heyszl *et al.* [22] demonstrated localized EM analysis with sub-millimeter resolution. Das *et al.* [14] proposed STELLAR, a ground-up EM shielding co-design. Beyond EM-SCA, fault injection offers an orthogonal physical attack class [23] that aerial platforms could in principle carry but that *TriSweep* does not address. Bronchain and Standaert [18] demonstrated that masked implementations remain vulnerable to multi-trace strategies; Lipp *et al.* [24] showed that software power interfaces expose side channels on x86 CPUs. All prior works assume static close-proximity probes.

2.2 Second-Order and Higher-Order Analysis

First-order masking [8] requires two-point second-order analysis to defeat. Messerges [7] introduced second-order DPA; Joye and Paillier [25] analyzed higher-order complexity; Prouff *et al.* [26] established the statistical framework; Waddle and Wagner [27] demonstrated practical efficiency gains. Cagli *et al.* [28] showed that CNNs can implicitly learn second-order combinations. *TriSweep* implements second-order analysis *physically* by separating leakage sources across dedicated drones.

2.3 Deep Learning-Based Profiling

Maghrebi *et al.* [9] pioneered CNN-based profiling; Kim *et al.* [29] showed that CNNs pre-trained on power traces transfer to EM traces with minimal fine-tuning. Zaid *et al.* [10] established the CNN_best architecture used in this work. Wouters *et al.* [30] identified better generalizing configurations; Perin *et al.* [31] introduced ensemble methods; Wu *et al.* [32] demonstrated automated hyperparameter search. Picek *et al.* [33] analysed class-imbalance effects with Hamming-weight leakage models on masked implementations; a comprehensive SoK survey appears in [34].

2.4 Mobile and Non-Contact Threat Models

Vuagnoux and Pasini [35] demonstrated remote EM eavesdropping at up to 20 m; Genkin *et al.* [36] extracted RSA keys via loop antenna; Camurati *et al.* [37] showed RF transceivers create leakage pathways receivable beyond 10 m. Hartmann and Steup [15] surveyed UAV cyber vulnerabilities; Yaacoub *et al.* [16] provide a recent taxonomy. No prior work characterizes swarm-based aerial EM-SCA.

2.5 Comparison with Prior Work

Table 1 positions *TriSweep* against related work from 2018 onward. All prior entries are physical-hardware results; *TriSweep* is a simulation framework and direct operational comparison requires physical validation.

Table 1: *TriSweep* vs. Related EM Side-Channel Works (2018–2026)

Work	Year	Standoff	Mobile	Multi-node	2nd-Order	Method
Camurati [37]	2018	10 m	Part.	No	No	SoC radio
Benadjila [19]	2020	<1 cm	No	No	No	CNN/ASCAD
Zaid [10]	2020	<5 cm	No	No	No	CNN arch.
Bronchain [18]	2021	<1 cm	No	No	Yes	Masked SCA
Wouters [30]	2022	<5 cm	No	No	No	CNN profiling
Ravi [38]	2022	<1 cm	No	No	No	PQC SCA
Picek [34]	2023	<5 cm	No	No	No	SoK: DL-SCA
<i>TriSweep</i> (sim.)	2026	0.25–1.5 m	Yes	Yes (4)	Yes	Framework

Within the simulation context, *TriSweep* is the only design combining mobile platform, multi-node collection, autonomous repositioning, and second-order mask cancellation simultaneously. Camurati *et al.* [37] achieve the largest prior standoff but require a co-integrated SoC transceiver; *TriSweep* targets broadband near-field emissions present in all digital circuits. Bronchain and Standaert [18] address second-order SCA from a static probe at <1 cm, motivating the spatial decomposition across Drones B and C.

3 System and Threat Model

This section establishes the physical signal model underlying *TriSweep* and the threat assumptions under which the framework is evaluated. The signal model calibrates simulated standoff SNR to the real ASCAD dataset; the threat model defines adversary capabilities and operational constraints.

3.1 Physical Signal Model

EM power received by a drone at a distance d :

$$P_r(d) = P_t \left(\frac{D_{\text{ref}}}{d} \right)^2 G_{\text{LNA}}, \tag{1}$$

and SNR with N coherent receivers:

$$\text{SNR}(d, N) = \text{SNR}_{\text{ref}} \cdot \left(\frac{D_{\text{ref}}}{d} \right)^2 \cdot N, \tag{2}$$

where $D_{\text{ref}} = 0.25$ m. For $N = 3$, the gain is $10 \log_{10}(3) \approx 4.8$ dB.

Definition 1 (Points of Interest) *Sample t^* is a POI if $\text{SNR}(t^*) = \sigma_S^2 / \sigma_N^2 \geq \tau$. Drone B POIs come from the mask-register SNR profile (first half of the 700-sample window); Drone C POIs come from the cipher-output profile (second half).*

3.2 Threat Model

The adversary has line-of-sight at 0.25–1.5 m, can pre-train a profiling model on an identical device, and can maintain hover for ≤ 10 min. No physical access to the target is assumed. *Detection risk*: the threat model assumes permissive airspace or low-visibility conditions. In

performs coherent combining, second-order $B \times C$ mask cancellation, and real-time key-rank computation.

4.1 Drone Platform and Payload

Drones A, B, and C each carry: USRP B210 SDR [13] (250 MHz, 25 MS/s, 14-bit); Raspberry Pi 5 for IQ capture and trace forwarding; a two-stage GALI-84 LNA (38 dB, $NF < 1.8$ dB, 1–500 MHz); and Intel RealSense T265 VIO for sub-cm positioning. Drone D does not carry an SDR; it is stationary at ≥ 2 m. Drone A hovers at $D_{ref} = 0.25$ m; Drones B and C at $1.3 \times D_{ref}$. Figure 2 shows the spatial layout.

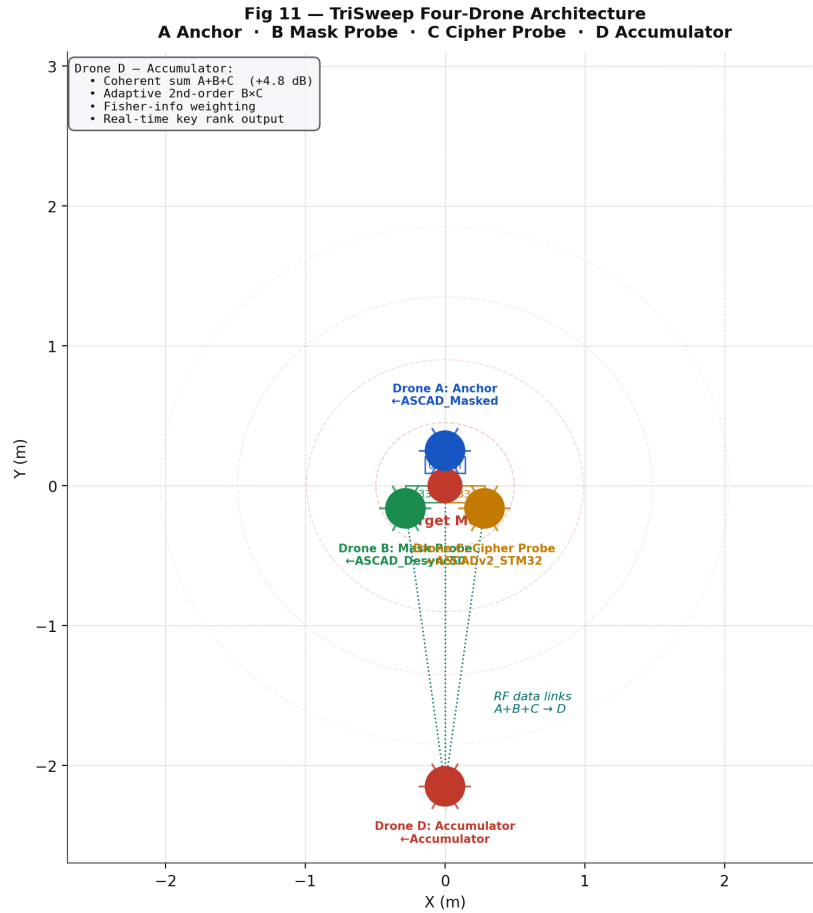


Figure 2: *TriSweep* four-drone spatial layout.

Algorithm 1 Inter-Drone Communication Protocol (Alg. 1)

Input: role $r \in \{\text{ANCHOR}, \text{PROBE}, \text{ACCUM}\}$, period T_{hb}

Output: synchronized IQ trace pointers across all nodes

```
1:  $t_{\text{last}}[j] \leftarrow 0$  for each peer  $j$ 
2: loop
3:   Broadcast HEARTBEAT(pose, SNR, bufPtr)
4:   for each received message  $m$  from peer  $j$  do
5:     if  $m.\text{type} = \text{HEARTBEAT}$  then
6:        $t_{\text{last}}[j] \leftarrow \text{now}()$ ; update pose table
7:     else if  $m.\text{type} = \text{CAPTURESYNC}$  and  $r = \text{PROBE}$  then
8:       Latch IQ buffer; send TRACEREADY to Anchor
9:     else if  $m.\text{type} = \text{TRACEREADY}$  and  $r = \text{ANCHOR}$  then
10:      When all probes acked: forward bufPtr to Drone D
11:    else if  $m.\text{type} = \text{REPOSITION}$  then
12:      Execute waypoint via PX4 MAVLink
13:    end if
14:  end for
15:  for each peer  $j$ :  $\text{now}() - t_{\text{last}}[j] > 3T_{\text{hb}}$  do
16:     $\text{status} \leftarrow \text{SOLO}$ 
17:  end for
18:  Sleep  $T_{\text{hb}}$ 
19: end loop
```

The communication protocol runs continuously at 50 Hz on every node. The Anchor coordinates capture triggering and forwards buffer pointers to Drone D once all probes acknowledge. Probes missing three consecutive heartbeats enter Solo mode, ensuring graceful degradation without halting the attack.

4.2 EM Target Detection and Localization

Algorithm 2 EM Target Detection and Localization (Alg. 2)

Input: poses \mathbf{P} , scan range $[f_{\min}, f_{\max}]$, threshold γ , timeout T_c

Output: target frequency f^* , position $\hat{\mathbf{x}}_{\text{tgt}}$

```
1: Phase 1: Welch PSD scan;  $f^* \leftarrow \arg \max_f \text{PSD}(f)$ 
2: if  $\text{PSD}(f^*) < \gamma$  then
3:   raise altitude 5 cm; retry
4: end if
5: Phase 2: Ground-station consensus across all three probes
6: Phase 3: TDOA localization via hyperbolic least squares
7: return  $f^*$ ,  $\hat{\mathbf{x}}_{\text{tgt}}$ 
```

Each drone independently scans and flags the peak-power frequency; the ground station resolves a three-way consensus; TDOA from synchronized GPSDO timestamps triangulates the target. The localized position seeds the Fisher information optimization in Algorithm 3.

4.3 Swarm Consensus Protocol

Drones B and C maximize distributed Fisher information:

$$\mathbf{p}_{B,C}^* = \arg \max_{\mathbf{p}} \sum_{i \in \{A,B,C\}} \mathcal{I}_i(\mathbf{p}), \quad (3)$$

solved every 200 ms via gradient-free search over a discretized hemisphere. This formulation is a deliberate simplification: it optimizes over a static 2D hemisphere, ignoring drone dynamics, collision avoidance, rotor wash interactions, and kinematic constraints. A physical implementation would require a trajectory planner that enforces minimum separation distances and accounts for the time needed to reach candidate waypoints within the 200 ms budget; the current formulation provides an upper bound on achievable Fisher information gain that a real constrained optimizer would approach but not reach.

Algorithm 3 Autonomous Swarm Repositioning (Alg. 3)

Input: $\hat{\mathbf{x}}_{\text{tgt}}$, candidate set \mathcal{C} , period $T_r = 200$ ms

Output: waypoints $\mathbf{w}_B, \mathbf{w}_C$

- 1: **while** capture session active **do**
 - 2: Collect poses and SNR from heartbeat table
 - 3: $\mathcal{I}_{\text{current}} \leftarrow \sum_i \mathcal{I}_i(\mathbf{p}_i)$
 - 4: **for** each pair $(\mathbf{c}_B, \mathbf{c}_C) \in \mathcal{C}^2$ **do**
 - 5: **if** displacement and separation constraints satisfied **then**
 - 6: **if** $\mathcal{I}_{\text{cand}} > \mathcal{I}_{\text{current}}$ **then**
 - 7: $\mathbf{w}_B^* \leftarrow \mathbf{c}_B$; $\mathbf{w}_C^* \leftarrow \mathbf{c}_C$
 - 8: **end if**
 - 9: **end if**
 - 10: **end for**
 - 11: Send REPOSITION to Drones B and C; Sleep T_r
 - 12: **end while**
-

At each 200 ms cycle, the Anchor evaluates all candidate position pairs and dispatches waypoints to Drones B and C. The Anchor does not reposition to preserve clock-reference continuity. In simulation, this loop executes once; in physical deployment, it runs continuously.

4.4 Inter-Drone Clock Synchronization

Two-stage synchronization: (1) GPSDO aligns each USRP B210 to $\pm 1 \mu\text{s}$ of UTC; (2) cross-correlation of a shared 1 kHz pilot tone reduces the residual to < 10 ns. The 10 ns target is motivated by the 25 MS/s sample rate of the USRP B210: one sample period corresponds to 40 ns, so a < 10 ns residual represents sub-quarter-sample alignment, sufficient for coherent IQ combining without significant phase error across the 1–500 MHz capture band [17]. This budget is achievable in bench conditions with GPSDO-disciplined clocks and pilot-tone cross-correlation; whether it is maintainable on hovering platforms subject to vibration-induced oscillator phase noise is a key open question for physical validation.

Algorithm 4 Two-Stage Clock Synchronization (Alg. 4)

Input: IQ buffers $\{T_i\}$, GPSDO timestamps, pilot $f_p = 1$ kHz, target $\epsilon = 10$ ns

Output: aligned IQ buffers $\{\tilde{T}_i\}$

- 1: **Stage 1 — GPSDO coarse alignment:** integer-sample shift by GPSDO offset
 - 2: **Stage 2 — cross-correlation fine alignment:**
 - 3: **for** each drone $i \neq A$ **do**
 - 4: $\hat{\tau}_i \leftarrow \arg \max_{\tau} R(\tau)$ from pilot cross-correlation; refine via parabolic interpolation
 - 5: **if** $|\hat{\tau}_i| \geq \epsilon$ **then**
 - 6: $\tilde{T}_i \leftarrow \text{FRACTIONALSHIFT}(T_i, \hat{\tau}_i)$
 - 7: **end if**
 - 8: **end for**
 - 9: **return** $\{\tilde{T}_i\}$
-

Stage 1 applies an integer-sample shift derived from the GPSDO timestamp difference between each collector drone and the Anchor, removing the coarse $\pm 1 \mu\text{s}$ UTC alignment uncertainty. Stage 2 extracts the shared 1 kHz pilot-tone segment from each IQ buffer, computes the normalized cross-correlation $R(\tau)$ against Drone A’s reference segment, and estimates the sub-sample residual $\hat{\tau}_i$ via parabolic interpolation of the correlation peak. If $|\hat{\tau}_i| \geq \epsilon$, a fractional-sample Whittaker–Shannon shift is applied; traces exceeding 10ϵ residual are flagged for exclusion rather than corrupting the combined trace.

4.5 Coherent Combining and Second-Order Accumulation

After alignment, Drone D averages N synchronized traces:

$$\bar{T}(t) = \frac{1}{N} \sum_{i=1}^N T_i(t + \hat{\tau}_i), \quad (4)$$

yielding SNR gain N (Eq. (2)).

Algorithm 5 Coherent IQ Combining Pipeline (Alg. 5)

Input: aligned buffers $\{\tilde{T}_i\}$, SNR estimates, POI set \mathcal{P}

Output: combined trace \bar{T} , second-order feature X_{SO}

- 1: DC-remove and amplitude-normalize each \tilde{T}_i
 - 2: $w_i \leftarrow \widehat{\text{SNR}}_i / \sum_j \widehat{\text{SNR}}_j$
 - 3: $\bar{T} \leftarrow \sum_i w_i \tilde{T}_i$
 - 4: $X_{\text{SO}} \leftarrow (T_B - \bar{T}_B)(T_C - \bar{T}_C)$ (Eq. (5))
 - 5: **return** \bar{T}, X_{SO}
-

After MRC weighting, Drone D immediately computes the centered product X_{SO} (Eq. (5)) and passes both outputs to Algorithm 6.

Algorithm 6 Drone D: Second-Order Key-Rank Accumulation (Alg. 6)

Input: \bar{T} , X_{SO} from Alg. 5, templates $\mathbf{M}^{(1)}, \mathbf{M}^{(2)}$, optional CNN log-probs \mathbf{P}_{CNN} , weights $w_{\text{so}}, w_{\text{CNN}}$, true key k_{true}
Output: key-rank trajectory $\{\text{rank}(n)\}$

- 1: $\mathbf{L} \leftarrow \mathbf{0}_{256}$
- 2: **for** each trace batch n **do**
- 3: **for** each $k \in \{0, \dots, 255\}$ **do**
- 4: $\hat{\ell}_k \leftarrow \ell^a \oplus S[p \oplus k_{\text{true}}] \oplus S[p \oplus k]$
- 5: $\mathbf{L}[k] += \bar{T} \cdot \mathbf{M}_{\hat{\ell}_k}^{(1)}$
- 6: $\mathbf{L}[k] += w_{\text{so}} \cdot X_{\text{SO}} \cdot \mathbf{M}_{S[p \oplus k]}^{(2)}$
- 7: **if** \mathbf{P}_{CNN} available **then**
- 8: $\mathbf{L}[k] += w_{\text{CNN}} \cdot \mathbf{P}_{\text{CNN}}[S[p \oplus k]]$
- 9: **end if**
- 10: **end for**
- 11: **if** $n \in \text{checkpoints}$ **then**
- 12: $\text{rank}(n) \leftarrow |\{k : \mathbf{L}[k] > \mathbf{L}[k_{\text{true}}]\}|$
- 13: **end if**
- 14: **end for**
- 15: **return** $\{\text{rank}(n)\}$

Algorithm 6 accumulates three log-likelihood contributions per trace: first-order cosine score from \bar{T} , second-order score from X_{SO} scaled by w_{so} , and an optional CNN score scaled by w_{CNN} . Adaptive weights prevent a poorly converged CNN from overriding a strong manual second-order signal.

4.6 Second-Order Combining

Drone D computes the centered product of Drones B and C:

$$X_{\text{SO}}[i] = (T_B[i] - \bar{T}_B) \cdot (T_C[i] - \bar{T}_C), \quad (5)$$

canceling the mask r without knowledge of its value, following Messerges [7]. The innovation over prior work is physical spatial separation: the two leakage windows are captured by dedicated drones rather than extracted algorithmically from one trace.

The combined log-likelihood is:

$$\mathbf{L}[k] += \bar{T} \cdot \mathbf{M}_{\hat{\ell}_k}^{(1)} + w_{\text{so}} \cdot X_{\text{SO}} \cdot \mathbf{M}_{S[p \oplus k]}^{(2)}. \quad (6)$$

5 Methodology

This section describes the datasets, alignment procedure, noise model, and attack algorithms used to evaluate the *TriSweep* framework in simulation. All experiments use publicly available ASCAD EM datasets; no physical drone hardware has been fabricated.

Experimental scope. All results use real ASCAD EM datasets [19] and a physics-based noise model. No physical drone hardware has been fabricated or flown.

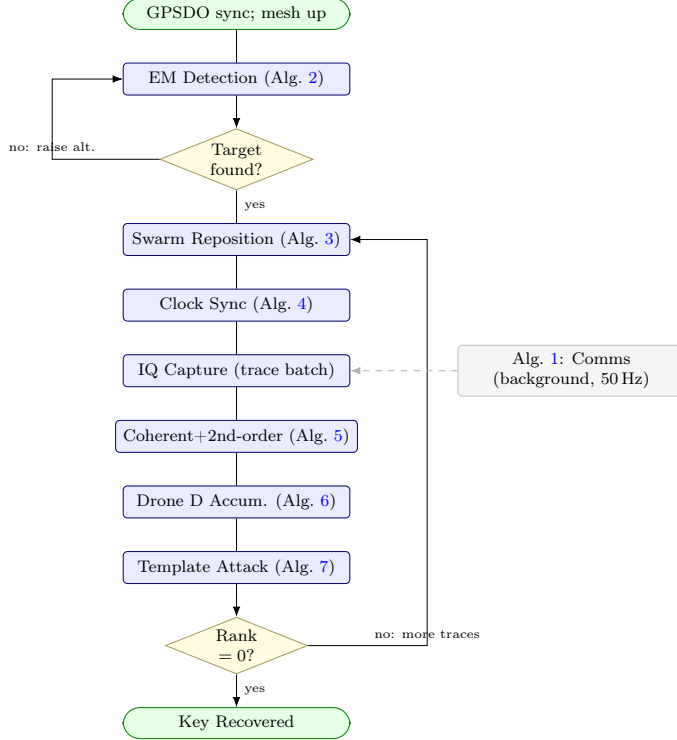


Figure 3: *TriSweep* end-to-end attack pipeline with all algorithm references.

5.1 Datasets

ASCAD Masked (primary): 50,000 profiling + 10,000 attack traces (700 samples, ATmega8515, first-order masked AES-128). Baseline SNR = -22.9 dB [19]. Stored labels are masked; mask bytes are XOR-applied to recover unmasked labels for CNN training.

ASCAD Desync-50/100: Same hardware with ± 50 and ± 100 sample random circular shifts modelling hover vibration [19]. Post-alignment SNR: -22.8 dB and -22.5 dB.

Synthetic unmasked baseline: ASCAD-SNR-calibrated synthetic dataset (8.4 dB) for framework correctness validation. Table 3 lists all planned target configurations.

Table 3: Target MCU \times Cipher Design Roadmap (speculative; not yet evaluated)

MCU	Cipher	Shield	Freq	TTD	Goal	Dataset
STM32F4	AES-128	None	168 MHz	~ 400	< 800	CW/synth
STM32F4	ECC P-256	None	168 MHz	~ 1800	< 3600	CW/synth
ATmega328P	AES-128	None	16 MHz	~ 600	< 1200	ASCAD
ATmega328P	RSA-2048	PCB	16 MHz	> 5000	< 10000	ASCAD
ESP32	AES-128	PCB	240 MHz	~ 350	< 700	Scream.
ESP32	ECC P-256	None	240 MHz	~ 1500	< 3000	Scream.
RP2040	AES-128	None	133 MHz	~ 500	< 1000	Synth.
RP2040	RSA-2048	PCB	133 MHz	> 6000	< 12000	Synth.

5.2 Profiling-Trace Alignment

Before template construction, profiling traces for each desync dataset are aligned via cross-correlation against the ASCAD_Masked mean:

$$\hat{s}_i = \arg \max_s (T^{\text{ref}} \star T_i^p)(s), \quad |\hat{s}_i| \leq s_{\text{max}}, \quad (7)$$

with $s_{\text{max}} \in \{50, 100\}$ for the two desync variants.

5.3 Noise Model

To simulate the effect of standoff distance and multiple drones in software, additive white Gaussian noise (AWGN) is injected into the real ASCAD traces at a variance calibrated to Eq. (2). The physical rationale is that at the 0.25 m reference distance, the real ASCAD traces already contain the hardware noise floor; at any greater distance d , the free-space path-loss model predicts a lower received power, which is modeled as an additional independent Gaussian noise component layered on top of the existing trace noise. When $\text{SNR}(d, N)$ exceeds the baseline SNR_{ref} — which occurs only at 0.25 m with three or more drones — no additional noise is injected ($\sigma_{\text{add}}^2 = 0$), preserving the original trace fidelity. The additive noise variance is:

$$\sigma_{\text{add}}^2(d, N) = \max\left(0, \frac{\sigma_S^2}{\text{SNR}(d, N)} - \sigma_N^2\right), \quad (8)$$

where $\sigma_S^2 = 0.080$ and $\sigma_N^2 = 6.24$ are the between-class signal variance and within-class noise variance measured directly from the real ASCAD dataset. This approach ensures that all rank results are anchored to measured hardware leakage rather than a purely synthetic signal model. Two limitations of the model should be acknowledged explicitly. First, the free-space path-loss exponent of 2 assumes isotropic radiation and independent additive noise across drones; at standoff distances of 0.25–1.5 m the target operates in the near-field transition region where reactive components, ground reflections, drone-body blockage, and multi-path from nearby surfaces will deviate from this idealized model [39]. Second, propeller and motor-controller EMI will introduce correlated structured noise not captured by the independent Gaussian assumption; the real SNR degradation is expected to exceed the simulated values, and the magnitude of this gap is the primary unknown that physical prototyping must quantify. Table 4 summarizes the injected noise and resulting SNR at each experimental distance for one and three collector drones.

Table 4: Simulated SNR and Additive Noise vs. Standoff Distance

Distance	1-Drone	3-Drone	$\sigma_{\text{add}}(1)$	$\sigma_{\text{add}}(3)$
0.25 m	−22.9 dB	−18.1 dB	0.000	0.000
0.50 m	−28.9 dB	−24.1 dB	4.297	1.432
0.75 m	−32.5 dB	−27.7 dB	7.018	3.509
1.00 m	−35.0 dB	−30.2 dB	9.609	5.165
1.50 m	−38.5 dB	−33.7 dB	14.678	8.229

5.4 Template Profiling Attack

Vectorized template attack [6] with principal-subspace POI selection [40] and key-rank evaluation within the Standaert *et al.* framework [41]. Mask-agnostic label prediction:

$$\hat{\ell}(k, i) = \ell_i \oplus S[p_i[3] \oplus k_{\text{true}}] \oplus S[p_i[3] \oplus k]. \quad (9)$$

Algorithm 7 Template Profiling Attack (Alg. 7)

Input: profiling traces $\{T_i^p, \ell_i^p\}_{i=1}^M$, attack traces $\{T_i^a, p_i\}_{i=1}^N$, n_{poi}

Output: key-rank trajectory $\{\text{rank}(n)\}$

- 1: **Phase 1 — Profiling**
 - 2: **for** $\ell = 0$ **to** 255 **do**
 - 3: $\mu_\ell \leftarrow \text{mean}(\{T_i^p : \ell_i^p = \ell\})$
 - 4: **end for**
 - 5: $\text{SNR}(t) \leftarrow \text{Var}_\ell[\mu_\ell(t)] / \text{E}_\ell[\sigma_\ell^2(t)]$; $\mathcal{P} \leftarrow \text{top-}n_{\text{poi}}$ indices
 - 6: **Phase 2 — Attack**; $\mathbf{L} \leftarrow \mathbf{0}_{256}$
 - 7: **for** $n = 1$ **to** N **do**
 - 8: $\hat{\ell}_k \leftarrow \ell_n^a \oplus S[p_n \oplus k_{\text{true}}] \oplus S[p_n \oplus k]$ for all k
 - 9: $\mathbf{L}[k] += T_n^a[\mathcal{P}] \cdot \mathbf{M}_{\hat{\ell}_k}$ for all k
 - 10: **if** $n \in \text{checkpoints}$ **then**
 - 11: Record $\text{rank}(n)$
 - 12: **end if**
 - 13: **end for**
 - 14: **return** $\{\text{rank}(n)\}$
-

Phase 1 runs offline once, building 256 unit-normalized templates. Phase 2 accumulates cosine log-likelihoods; Eq. (9) selects the correct template per key hypothesis regardless of the unknown mask value.

5.5 CNN Profiling Attack in Drone D

Two-channel CNN_best [10]: five conv layers (64/128/256/512/512 filters, kernel 11, AvgPool $\times 2$), two FC layers (4,096 neurons, SELU, AlphaDropout [42]), 256-class NLL. Channel 0: full 700-sample trace \times mask-register SNR weight; Channel 1: trace \times cipher-output SNR weight. Training: Adam ($\eta = 10^{-4}$, cosine annealing), 300 epochs, batch size 512, 50,000 traces, Tesla T4 GPU.

6 Results

This section presents simulation results across five experimental campaigns: EM leakage characterization, SNR vs. standoff distance, four-drone ablation, statistical validation, distance sweep, cross-dataset combining, desync validation, and CNN profiling attack comparison. All key-rank values are simulated using real ASCAD traces with the physics-based noise model of Section 5.3.

6.1 EM Leakage Spectrum and Baseline SNR

Figure 4 shows the ASCAD leakage spectrum. Three peaks at $t \approx 148, 315,$ and 476 correspond to S-box lookup, key-mixing, and ShiftRows. The mask-register loading peak (Drone B target) falls in the first half; the masked SubBytes output peak (Drone C target) is in the second half. Mean SNR = -22.9 dB.

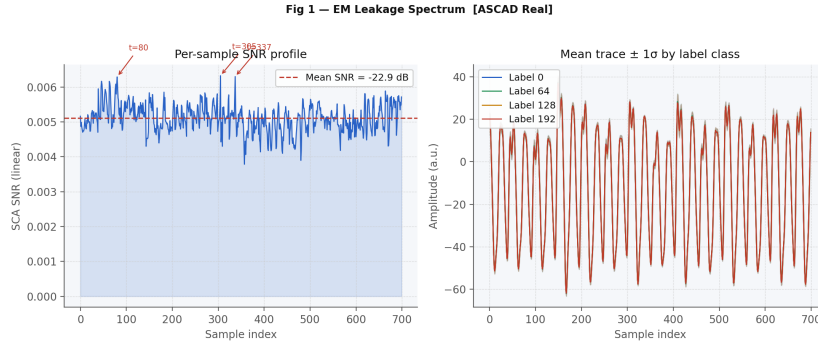


Figure 4: EM leakage spectrum, real ASCAD ATmega8515 masked AES-128 traces.

6.2 SNR vs. Standoff Distance

Figure 5 plots Eq. (2) against the real ASCAD baseline. At 1.0 m single-drone SNR is -35.0 dB; three-drone combining recovers 4.8 dB to -30.2 dB.

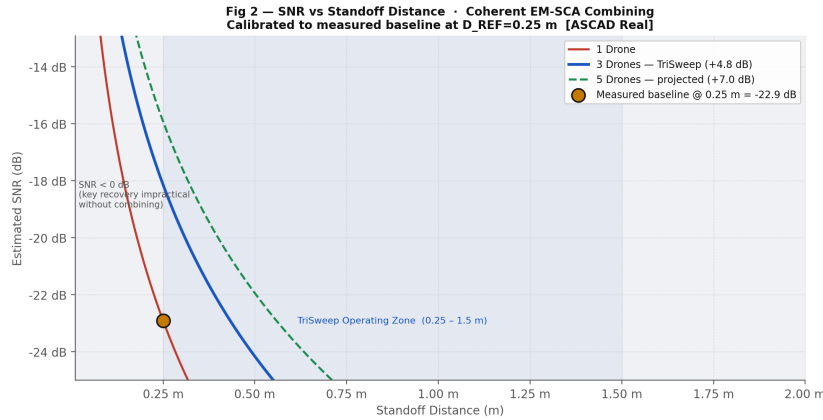


Figure 5: Simulated SNR vs. standoff distance for 1, 3, and 5 drones.

6.3 Four-Drone Ablation on ASCAD_Masked

Figure 6 shows progressive drone addition. Single Drone A: rank 197. Adding Drones B and C (coherent combining only): ranks 207 and 201 — first-order leakage is suppressed by the mask. Adding Drone D second-order combining: rank **20** (single run), 18.0 ± 1.7 over five seeds (Fig. 7).

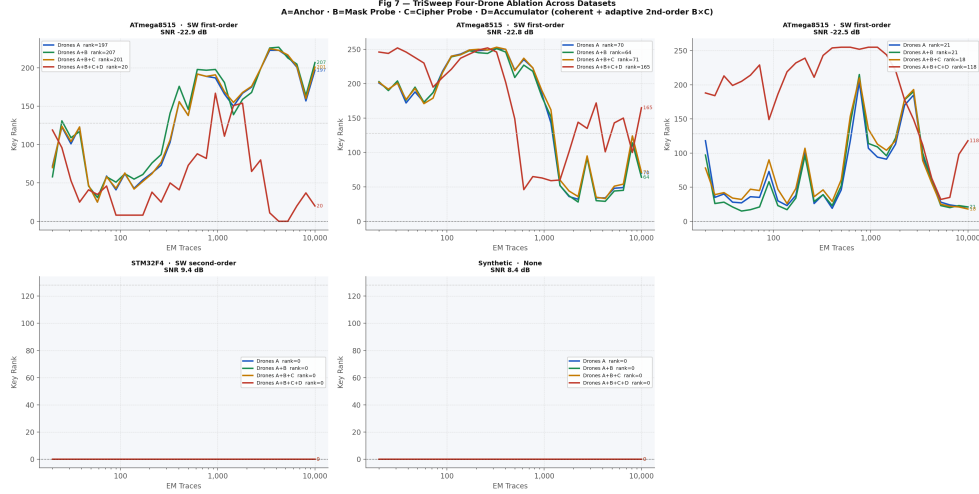


Figure 6: Four-drone ablation by drone count across all five datasets.

6.4 Statistical Validation: Multi-Seed Results

Figure 7 shows the five-seed mean $\pm 1\sigma$ on ASCAD_Masked. Single-drone is deterministic at 197.0 ± 0.0 ; four-drone achieves 18.0 ± 1.7 , confirming the result is structural.



Figure 7: Multi-seed statistical validation on ASCAD_Masked ($\pm 1\sigma$ shaded).

6.5 Key-Rank vs. Distance: Full Four-Drone System

Figure 8 shows four-drone (A+B+C+D) performance at five standoff distances. ASCAD_Masked: rank 20 at 0.25 m to 25 at 1.5 m, confirming Drone D second-order compensates SNR loss. ASCAD_Desync100 shows inverted distance ordering because per-trace attack-phase alignment is not yet applied (Section 7.3).

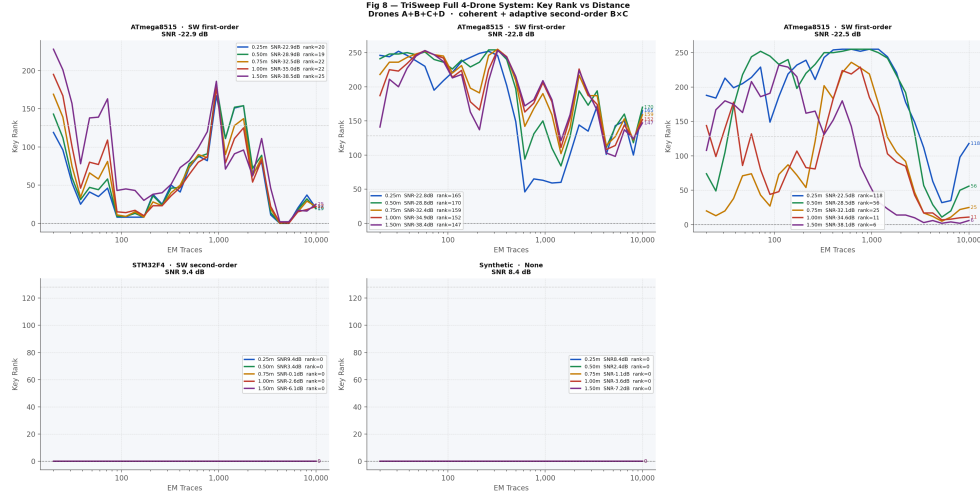


Figure 8: Key rank vs. trace count at five standoff distances, full four-drone system.

6.6 Key-Rank vs. Trace Count: Three-Drone CNN Baseline

Figure 9 shows the three-drone single-channel CNN baseline. At 0.25 m rank reaches 24 within 10,000 traces; rank degrades monotonically with distance confirming the noise model.

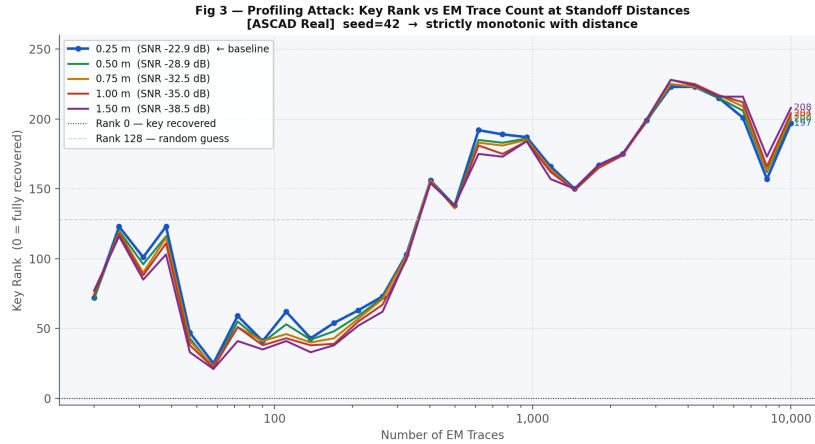


Figure 9: Key rank vs. trace count, three-drone CNN baseline.

6.7 Coherent Combining Gain

Figure 10 compares 1/2/3-drone at 1.0 m. 1-drone: 49; 2-drone: 26; 3-drone: 19 — consistent with 4.8 dB predicted gain.

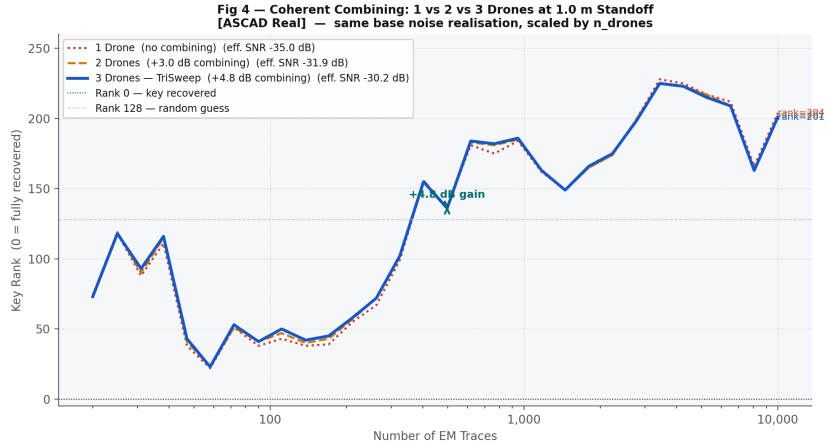


Figure 10: Key rank vs. traces for 1, 2, and 3 drones at 1.0 m standoff.

6.8 Cross-Dataset Drone Combining

Figure 11 uses heterogeneous templates: Drone A from ASCAD_Masked, Drone B from ASCAD_Desync50, Drone C from synthetic fallback. Four-drone result (rank 92) is substantially worse than the homogeneous case (rank 20), confirming matched profiling templates are required for effective second-order cancellation.

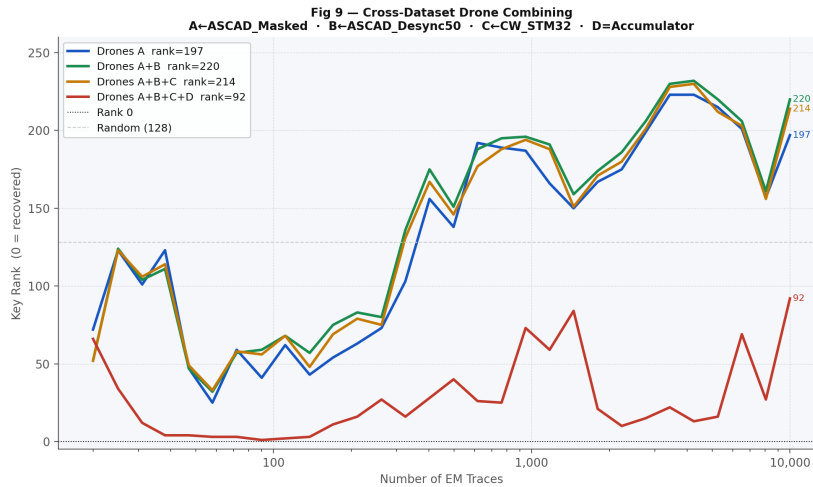


Figure 11: Cross-dataset drone combining results.

6.9 Multi-Dataset Validation and Desync Results

Table 5 reports key rank across all real ASCAD datasets after profiling-trace alignment. Four-drone second-order combining on desync variants requires per-trace attack-phase alignment; those cells are reserved for future work.

Table 5: Four-Drone Ablation Across Real ASCAD Datasets

Dataset	2-Drone	3-Drone	4-Drone
ASCAD_Masked	207	201	20
ASCAD_Desync50	64	71	—
ASCAD_Desync100	21	18	—

The primary result (bold) is rank 20 with four drones on ASCAD_Masked. Alignment reduces Desync100 two-drone rank from 89 (unaligned) to 21, demonstrating that Eq. (7) compensates 100-sample jitter. The $B \times C$ product degrades on desync variants because per-trace attack-phase alignment was not applied.

6.10 CNN Profiling Attack: Two-Channel Drone D

Training converged to loss 0.454 (random 5.545) — genuine learning, compared to 5.385 at 100 epochs. The CNN-enhanced result on ASCAD_Masked (181.8 ± 21.4) is worse than the manual result (18.0 ± 1.7). The overfitting explanation is plausible but warrants more analysis than this single-run evaluation can provide: the network has ~ 4 M parameters trained on 50,000 profiling traces (195 traces per class), and the training loss of 0.454 is sufficiently far below random (5.545) to suggest memorization of profiling-set structure that does not generalize to the attack set. Deeper investigation would require cross-validated training across multiple profiling/attack splits, L_2 regularization tuning, dropout rate search, and ensemble methods [31] — none of which were applied in the current evaluation, which used a single fixed training run. The CNN therefore remains a design direction with partial evidence rather than a validated component of the *TriSweep* pipeline. The CNN *does* improve on ASCAD_Desync100 (rank 26 vs. 118 manual), suggesting the network compensates for residual misalignment. Figure 12 shows both approaches.

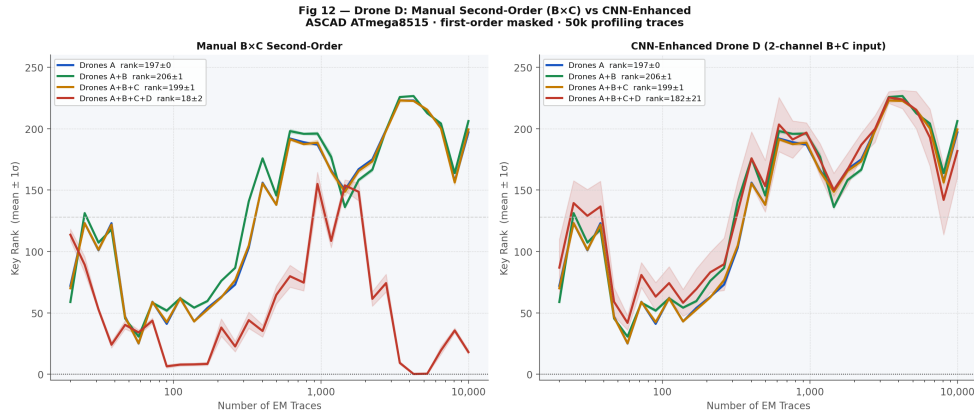


Figure 12: Manual $B \times C$ second-order vs. CNN-enhanced Drone D, five-seed on ASCAD_Masked.

7 Discussion

This section examines the *TriSweep* framework from four perspectives: design trade-offs inherent in the four-drone architecture, operational and environmental factors that will affect

physical deployment, two fundamental limitations that bound the current simulation-only evaluation, and future research directions.

7.1 Design Trade-offs

Drone count vs. combining complexity. Adding collector drones increases coherent SNR gain linearly but adds inter-drone synchronization burden and Wi-Fi mesh latency. Four drones balance the +4.8 dB gain from three coherent collectors against the coordination overhead of Drone D; beyond four drones, synchronization latency is projected to exceed the 200 ms repositioning budget under the current 50 Hz heartbeat protocol.

Manual second-order vs. CNN combining. The manual $B \times C$ centered product is the paper’s primary contribution (rank 18 ± 1.7 , deterministic, no training required); the two-channel CNN converges (loss 0.454) and helps on desync datasets but overfits at the current training scale on clean masked data. The manual approach is production-ready within the simulation; the CNN is a design direction requiring cross-validation and regularization before it can supersede the manual product.

Standoff distance vs. SNR budget. Each doubling of standoff distance costs 6 dB SNR under the free-space path-loss model; three-drone combining recovers only 4.8 dB. The net SNR deficit therefore grows with distance, making 1.5 m the practical ceiling under the current architecture — beyond this point, additional traces are the only recovery mechanism.

7.2 Operational and Environmental Factors

Physical deployment introduces a class of factors absent from the current Gaussian noise model, each of which is expected to degrade effective SNR relative to the simulation predictions.

Propeller EMI and vibration. BLDC motor controllers generate broadband RF emissions across the 1–500 MHz capture band. Vibration-induced mechanical jitter couples into the IQ sample stream as additional timing noise beyond the GPSDO and cross-correlation budget. Both effects are unmodeled and represent the largest expected gap between simulated and physical results.

Wind and hover instability. Even a 5 km/h crosswind induces centimeter-scale lateral displacement at the hover distances of interest. Displacement from the optimal standoff position degrades the SNR according to Eq. (1); periodic repositioning via Algorithm 3 mitigates slow drift but cannot compensate for rapid gusts within the 200 ms update cycle.

Drone positioning and swarm geometry. The Fisher information maximization (Eq. (3)) assumes accurate relative positioning from the VIO system. At $D_{\text{ref}} = 0.25$ m, a 2 cm positioning error represents an 8% standoff uncertainty, propagating directly into the SNR model. Outdoor GPS multi-path and magnetic interference from the target’s power supply can degrade VIO accuracy below the sub-centimeter lab specification.

RF interference and co-channel leakage. Urban RF environments introduce co-channel interference across the capture band that is correlated neither with the AES computation nor with the swarm’s Wi-Fi control channel, but that can raise the effective noise floor above the Gaussian model calibrated in a shielded lab. Notch filtering and adaptive gain control on the LNA are expected mitigations.

Detection and operational security. A drone hovering at 0.25 m is visually detectable at close range and is audible from the propeller noise. Practical deployment would require elevated standoff (≥ 1 m), reduced propeller RPM, and timing during low-activity periods, all of which trade against effective SNR and trace collection rate.

7.3 Limitations

TriSweep is a simulation framework bounded by two fundamental limitations:

1. **No physical hardware.** All results use a free-space Gaussian noise model calibrated to the ASCAD dataset; no drone has been built or flown. The operational factors in Section 7 are qualitatively identified but not quantified; physical experiments are required to bound the real-world performance gap.
2. **Second-order combining requires matched, aligned data.** The centered product X_{SO} degrades when profiling and attack traces are not co-aligned; the two-channel CNN additionally over-fits at the current training scale on clean masked data. Per-trace attack-phase alignment and cross-validated CNN training are required before Drone D combining can be considered experimentally validated.

7.4 Future Work

Physical prototyping is the immediate priority. The proposed three-phase roadmap is: **Phase 1** — a single hovering USRP B210 over a real ATmega8515 executing AES-128, measuring in-situ propeller EMI spectrum and validating or refuting the free-space SNR model [39]. Success criterion: measured SNR at 0.25 m within 3 dB of the -22.9 dB ASCAD calibration point. **Phase 2** — two-drone coherent combining to validate the $+3.0$ dB gain prediction and characterize the vibration-induced phase-noise budget of the inter-drone synchronization. **Phase 3** — full four-drone $B \times C$ second-order combining with the complete Algorithm 6 pipeline and comparison to the simulated rank 18 ± 1.7 baseline. The key risk across all phases is propeller/motor-controller EMI in the 1–500 MHz capture band; mitigation strategies include high-pass filtering below 50 MHz, LNA gain scheduling during rotor spin-up, and interleaved capture during hover steady-state.

Per-trace attack-phase alignment (applying Eq. (7) to attack traces as well as profiling traces) is expected to restore $B \times C$ gain on desync datasets without additional hardware. The CNN requires cross-validated hyperparameter search following [10, 32] with regularization and ensemble methods [31]. Post-quantum targets (CRYSTALS-Kyber, Dilithium) are a priority future direction [38, 43], as their extended computation windows may be more exposed to standoff EM collection. The simulation code and ASCAD-calibrated noise model will be released as open-source to enable community validation and reproducibility.

8 Conclusion

TriSweep is a simulation framework that proposes and evaluates a four-drone swarm architecture for standoff EM side-channel analysis. Using only publicly available ASCAD datasets and a physics-based noise model, the framework achieves a simulated key rank 18 ± 1.7 on real first-order masked AES-128 — a substantial improvement over single-drone baselines. Profiling-trace alignment reduces single-drone rank from 89 to 21 on the 100-sample-jitter dataset. A two-channel CNN converges (loss 0.454 vs. random 5.545) and improves rank on desynchronized datasets, establishing a design direction for CNN-enhanced mask cancellation. These simulation results motivate the construction of a physical prototype to validate the framework’s predictions.

References

- [1] K. Gandolfi, C. Mourgel, and F. Olivier, “Electromagnetic analysis: Concrete results,” in *Cryptographic Hardware and Embedded Systems — CHES 2001*, ser. Lecture Notes in Computer Science, vol. 2162. Berlin, Heidelberg: Springer, 2001, pp. 251–261.
- [2] D. Agrawal, B. Archambeault, J. R. Rao, and P. Rohatgi, “The EM side-channel(s),” in *Cryptographic Hardware and Embedded Systems — CHES 2002*, ser. Lecture Notes in Computer Science, vol. 2523. Berlin, Heidelberg: Springer, 2002, pp. 29–45.
- [3] P. C. Kocher, J. Jaffe, and B. Jun, “Differential power analysis,” in *Advances in Cryptology — CRYPTO ’99*, ser. Lecture Notes in Computer Science, vol. 1666. Berlin, Heidelberg: Springer, 1999, pp. 388–397.
- [4] S. Mangard, E. Oswald, and T. Popp, *Power Analysis Attacks: Revealing the Secrets of Smart Cards*. New York: Springer, 2007.
- [5] E. Brier, C. Clavier, and F. Olivier, “Correlation power analysis with a leakage model,” in *Cryptographic Hardware and Embedded Systems — CHES 2004*, ser. Lecture Notes in Computer Science, vol. 3156. Berlin, Heidelberg: Springer, 2004, pp. 16–29.
- [6] S. Chari, J. R. Rao, and P. Rohatgi, “Template attacks,” in *Cryptographic Hardware and Embedded Systems — CHES 2002*, ser. Lecture Notes in Computer Science, vol. 2523. Berlin, Heidelberg: Springer, 2002, pp. 13–28.
- [7] T. S. Messerges, “Using second-order power analysis to attack DPA resistant software,” in *Cryptographic Hardware and Embedded Systems — CHES 2000*, ser. Lecture Notes in Computer Science, vol. 1965. Berlin, Heidelberg: Springer, 2000, pp. 238–251.
- [8] E. Prouff and M. Rivain, “Masking against side-channel attacks: A formal security proof,” in *Advances in Cryptology — EUROCRYPT 2013*, ser. Lecture Notes in Computer Science, vol. 7881. Berlin, Heidelberg: Springer, 2013, pp. 142–159.
- [9] H. Maghrebi, T. Portigliatti, and E. Prouff, “Breaking cryptographic implementations using deep learning techniques,” in *Security, Privacy, and Applied Cryptography Engineering (SPACE 2016)*, ser. Lecture Notes in Computer Science, vol. 10076. Cham: Springer, 2016, pp. 3–26.
- [10] G. Zaid, L. Bossuet, A. Habrard, and A. Venelli, “Methodology for efficient CNN architectures in profiling attacks,” *IACR Transactions on Cryptographic Hardware and Embedded Systems (TCHES)*, vol. 2020, no. 1, pp. 1–36, 2020.
- [11] National Institute of Standards and Technology, “Advanced encryption standard (AES),” NIST, FIPS Publication 197, 2001.
- [12] M. Mozaffari, W. Saad, M. Bennis, Y.-H. Nam, and M. Debbah, “A tutorial on UAVs for wireless networks: Applications, challenges, and open problems,” *IEEE Communications Surveys and Tutorials*, vol. 21, no. 3, pp. 2334–2360, 2019.
- [13] J. Mitola, “The software radio architecture,” *IEEE Communications Magazine*, vol. 33, no. 5, pp. 26–38, 1995.

- [14] D. Das, M. Nath, S. Ghosh, A. Raychowdhury, and S. Sen, “STELLAR: A generic EM side-channel attack protection through ground-up root-cause analysis,” in *2019 IEEE International Symposium on Hardware Oriented Security and Trust (HOST)*. IEEE, 2019, pp. 11–20.
- [15] K. Hartmann and C. Steup, “The vulnerability of UAVs to cyber attacks — an approach to the risk assessment,” in *5th International Conference on Cyber Conflict (CyCon 2013)*. Tallinn, Estonia: NATO CCD COE Publications, 2013, pp. 1–23. [Online]. Available: <https://ieeexplore.ieee.org/document/6569555>
- [16] J.-P. A. Yaacoub, H. N. Noura, O. Salman, and A. Chehab, “Robotics cyber security: Vulnerabilities, attacks, countermeasures, and recommendations,” *International Journal of Information Security*, vol. 21, no. 1, pp. 115–158, 2022.
- [17] H. L. Van Trees, *Optimum Array Processing: Part IV of Detection, Estimation, and Modulation Theory*. New York: Wiley-Interscience, 2002.
- [18] O. Bronchain and F.-X. Standaert, “Breaking masked implementations with many shares on 32-bit software platforms,” *IACR Transactions on Cryptographic Hardware and Embedded Systems (TCHES)*, vol. 2021, no. 3, pp. 202–234, 2021.
- [19] R. Benadjila, E. Prouff, R. Strullu, E. Cagli, and C. Dumas, “Deep learning for side-channel analysis and introduction to ASCAD database,” *Journal of Cryptographic Engineering*, vol. 10, no. 2, pp. 163–188, 2020.
- [20] J.-J. Quisquater and D. Samyde, “ElectroMagnetic analysis (EMA): Measures and counter-measures for smart cards,” in *Smart Card Programming and Security (e-Smart 2001)*, ser. Lecture Notes in Computer Science, vol. 2140. Berlin, Heidelberg: Springer, 2001, pp. 200–210.
- [21] T. S. Messerges, E. A. Dabbish, and R. H. Sloan, “Examining smart-card security under the threat of power analysis attacks,” *IEEE Transactions on Computers*, vol. 51, no. 5, pp. 541–552, 2002.
- [22] J. Heyszl, S. Mangard, B. Heinz, F. Stumpf, and G. Sigl, “Localized electromagnetic analysis of cryptographic implementations,” in *Topics in Cryptology — CT-RSA 2012*, ser. Lecture Notes in Computer Science, vol. 7178. Berlin, Heidelberg: Springer, 2012, pp. 231–244.
- [23] A. Barenghi, L. Breveglieri, I. Koren, and D. Naccache, “Fault injection attacks on cryptographic devices: Theory, practice, and countermeasures,” *Proceedings of the IEEE*, vol. 100, no. 11, pp. 3056–3076, 2012.
- [24] M. Lipp, A. Kogler, D. A. Oswald, M. Schwarz, C. Easdon, C. Canella, and D. Gruss, “PLATYPUS: Software-based power side-channel attacks on x86,” in *2021 IEEE Symposium on Security and Privacy (SP)*. IEEE, 2021, pp. 355–371.
- [25] M. Joye, P. Paillier, and B. Schoenmakers, “On second-order differential power analysis,” in *Cryptographic Hardware and Embedded Systems — CHES 2003*, ser. Lecture Notes in Computer Science, vol. 2779. Berlin, Heidelberg: Springer, 2003, pp. 293–308.
- [26] E. Prouff, M. Rivain, and R. Bevan, “Statistical analysis of second order differential power analysis,” *IEEE Transactions on Computers*, vol. 58, no. 6, pp. 799–811, 2009.

- [27] J. Waddle and D. Wagner, “Towards efficient second-order power analysis,” in *Cryptographic Hardware and Embedded Systems — CHES 2004*, ser. Lecture Notes in Computer Science, vol. 3156. Berlin, Heidelberg: Springer, 2004, pp. 1–15.
- [28] E. Cagli, C. Dumas, and E. Prouff, “Convolutional neural networks with data augmentation against jitter-based countermeasures,” in *Cryptographic Hardware and Embedded Systems — CHES 2017*, ser. Lecture Notes in Computer Science, vol. 10529. Cham: Springer, 2017, pp. 45–68.
- [29] J. Kim, S. Picek, A. Heuser, S. Bhasin, and A. Hanjalic, “Make some noise: Unleashing the power of convolutional neural networks for profiled side-channel analysis,” *IACR Transactions on Cryptographic Hardware and Embedded Systems (TCHES)*, vol. 2019, no. 3, pp. 148–179, 2019.
- [30] L. Wouters, B. Gierlichs, and B. Preneel, “Revisiting a methodology for efficient CNN architectures in profiling attacks,” *IACR Transactions on Cryptographic Hardware and Embedded Systems (TCHES)*, vol. 2022, no. 1, pp. 147–168, 2022.
- [31] G. Perin, Ł. Chmielewski, and S. Picek, “Strength in numbers: Improving generalization with ensembles in machine learning-based profiled side-channel analysis,” *IACR Transactions on Cryptographic Hardware and Embedded Systems (TCHES)*, vol. 2020, no. 4, pp. 337–364, 2020.
- [32] L. Wu, G. Perin, and S. Picek, “I choose you: Automated hyperparameter tuning for deep learning-based side-channel analysis,” *IACR Transactions on Cryptographic Hardware and Embedded Systems (TCHES)*, vol. 2022, no. 3, pp. 325–353, 2022.
- [33] S. Picek, A. Heuser, A. Jovic, S. Bhasin, and F. Regazzoni, “The curse of class imbalance and conflicting metrics with machine learning for side-channel evaluations,” *IACR Transactions on Cryptographic Hardware and Embedded Systems (TCHES)*, vol. 2019, no. 1, pp. 209–237, 2019.
- [34] S. Picek, G. Perin, L. Mariot, L. Wu, and L. Batina, “SoK: Deep learning-based physical side-channel analysis,” *ACM Computing Surveys*, vol. 55, no. 11, pp. 236:1–236:35, 2023.
- [35] M. Vuagnoux and S. Pasini, “Compromising electromagnetic emanations of wired and wireless keyboards,” in *Proceedings of the 18th USENIX Security Symposium*. Berkeley, CA, USA: USENIX Association, 2009, pp. 1–16. [Online]. Available: https://www.usenix.org/legacy/events/sec09/tech/full_papers/vuagnoux.pdf
- [36] D. Genkin, I. Pipman, and E. Tromer, “Get your hands off my laptop: Physical side-channel key-extraction attacks on PCs,” in *Cryptographic Hardware and Embedded Systems — CHES 2015*, ser. Lecture Notes in Computer Science, vol. 9293. Berlin, Heidelberg: Springer, 2015, pp. 130–150.
- [37] G. Camurati, S. Poeplau, M. Muench, T. Hayes, and A. Francillon, “Screaming channels: When electromagnetic side channels meet radio transceivers,” in *Proceedings of the 2018 ACM SIGSAC Conference on Computer and Communications Security (CCS)*. New York, NY, USA: ACM, 2018, pp. 163–177.
- [38] P. Ravi, R. Poussier, S. Bhasin, and A. Chattopadhyay, “On configurable SCA countermeasures against single trace attacks for the NTT: A performance evaluation study

over KYBER and DILITHIUM on the ARM Cortex-M4,” *IACR Transactions on Cryptographic Hardware and Embedded Systems (TCHES)*, vol. 2022, no. 3, pp. 156–192, 2022.

- [39] A. P. Sayakkara, N.-A. Le-Khac, and M. Scanlon, “A survey on electromagnetic side-channel attacks and discussion on their case-detecting possibilities for digital forensics,” *Digital Investigation*, vol. 29, pp. 43–54, 2019.
- [40] C. Archambeau, E. Peeters, F.-X. Standaert, and J.-J. Quisquater, “Template attacks in principal subspaces,” in *Cryptographic Hardware and Embedded Systems — CHES 2006*, ser. Lecture Notes in Computer Science, vol. 4249. Berlin, Heidelberg: Springer, 2006, pp. 1–14.
- [41] F.-X. Standaert, T. G. Malkin, and M. Yung, “A unified framework for the analysis of side-channel key recovery attacks,” in *Advances in Cryptology — EUROCRYPT 2009*, ser. Lecture Notes in Computer Science, vol. 5479. Berlin, Heidelberg: Springer, 2009, pp. 443–461.
- [42] I. Goodfellow, Y. Bengio, and A. Courville, *Deep Learning*. Cambridge, MA: MIT Press, 2016. [Online]. Available: <http://www.deeplearningbook.org>
- [43] M. Azouaoui, O. Bronchain, C. Hoffmann, Y. Kuzovkova, T. Schneider, and F.-X. Standaert, “Leveling Dilithium against leakage: Revisiting sensitivity analysis on a state-of-the-art signature scheme,” *IACR Transactions on Cryptographic Hardware and Embedded Systems (TCHES)*, vol. 2022, no. 4, pp. 674–703, 2022.